2016

Evidence of the Excitation of a Ring-Like Gravity Wave in the Mesosphere over the Andes Lidar Observatory

Fabio Vargas
University of Illinois at Urbana-Champaign / National Institute for Space Research

Gary Swenson,
University of Illinois at Urbana-Champaign

Alan Liu
Embry-Riddle Aeronautical University, liuz2@erau.edu

Dominique Pautet

Scholarly Commons Citation

Vargas, F., G. Swenson, A. Liu, and D. Pautet (2016), Evidence of the excitation of a ring-like gravity wave in the mesosphere over the Andes Lidar Observatory, J. Geophys. Res. Atmos., 121, doi:10.1002/2016JD024799

AGU PUBLICATIONS

JGR

Journal of Geophysical Research: Atmospheres

RESEARCH ARTICLE
10.1002/2016JD024799

Key Points:
- Shows a rare ring-like gravity wave event
- Several instruments reveal different aspects of the wave
- It is a unique secondary wave excitation example

Supporting Information:
- Supporting Information S1
- Movie S1
- Movie S2

Correspondence to:
F. Vargas,
fvargas@illinois.edu

Citation:
Vargas, F., G. Swenson, A. Liu, and D. Pautet (2016), Evidence of the excitation of a ring-like gravity wave in the mesosphere over the Andes Lidar Observatory, *J. Geophys. Res. Atmos.*, *121*, doi:10.1002/2016JD024799.

Received 17 JAN 2016
Accepted 15 JUN 2016
Accepted article online 22 JUN 2016

Evidence of the excitation of a ring-like gravity wave in the mesosphere over the Andes Lidar Observatory

Fabio Vargas[1], Gary Swenson[1], Alan Liu[2], and Dominique Pautet[3]

[1]Remote Sensing and Space Science Laboratory, University of Illinois at Urbana-Champaign, Urbana, Illinois, USA, [2]Department of Physical Sciences, Embry-Riddle Aeronautical University, Daytona Beach, Florida, USA, [3]Physics Department, Utah State University, Logan, Utah, USA

Abstract On 23 March 2012, our all-sky imager recorded a concentric, ring-like gravity wave pattern. The wave arose within the area covered by images of both OH and O(^1S) nightglow emissions taken at the Andes Lidar Observatory (ALO), Chile (30.3°S, 70.7°W). We have estimated the observed and intrinsic parameters of the event and located the wave source within the lower mesosphere altitude range using a reverse ray tracing method. By the analysis of GOES and LIS satellite images, we have not found evidence of neither convective nor lightning activity nearby ALO, indicating that the source of the ring-like wave was not directly in the troposphere. The absence of tropospheric activity and the height of the source of the event suggest that a secondary wave generation mechanism might be the cause of the ring-like wave. The secondary wave mechanism was likely triggered by a breaking, larger-scale primary wave excited by deep convection ~1400 km northeast of ALO over Bolivia, as determined by a forward ray tracing scheme.

1. Introduction

The excitation of gravity waves (GWs) takes place at several altitudes throughout the atmosphere under proper conditions of stability and dynamics. From the ground up to the tropopause, latent heat release in convective fronts and orography forcing are the primary excitation mechanisms of GWs [*Fritts et al.*, 2006]. Above the tropopause, wind shear, geostrophic adjustment, and body forcing are most effective in populating the gravity wave spectrum observed at higher altitudes [*Fritts et al.*, 2006]. These excitation mechanisms are ubiquitous on the Earth, and observation efforts strive to understand the impact of the propagating waves on the middle atmosphere circulation, energetic balance, and constituent transport.

The imagery of the mesospheric nightglows via all-sky cameras is commonly applied to observe planar GWs [e.g., *Taylor et al.*, 1987; *Pautet et al.*, 2005]. It is a powerful technique to watch atmospheric gravity waves and allows accessing the spatial and temporal features of these perturbations forthrightly [e.g., *Vargas et al.*, 2009; *Bageston*, 2009]. As GWs disturb the atmospheric fields (temperature and density), they alter the nightglow photochemical reactions and the observed nightglow radiance [*Tarasick and Hines*, 1990]; imaging systems record the radiance fluctuations associated with the wave oscillations [*Swenson and Gardner*, 1998]. Large vertical wavelength, large speed, and high-frequency waves are more readily observed in the imagery of the nightglow emissions [*Liu and Swenson*, 2003; *Vargas et al.*, 2007]. The high-frequency waves are important in transporting horizontal momentum flux vertically and dramatically alter the local background flow when they break, eventually triggering a broad spectrum of secondary gravity waves. The frequency of these secondary waves depend on the frequency of the primary, breaking waves [*Vadas and Fritts*, 2001; *Snively and Pasko*, 2003].

Although planar GWs are frequent, only a few reports of concentric, ring-like wavefronts observed with ground-based airglow imagers are found in the literature [*Taylor and Hapgood*, 1988; *Smith et al.*, 2006; *Sentman et al.*, 2003; *Suzuki et al.*, 2007; *Yue et al.*, 2009; *Vadas et al.*, 2012; *Yue et al.*, 2013; *Xu et al.*, 2015]. Usually, these concentric wave events are associated with deep convection as their excitation source. For instance, *Vadas et al.* [2009] modeled the *Yue et al.* [2009] waves and proposed that their excitation was caused by the overshoot of convective updraft envelopes into the stable stratosphere at ~20 km height. These envelopes would preserve their shape under a weak background flow and reach mesospheric altitudes as

curved wavefronts. Concentric gravity waves observed simultaneously in lower atmosphere and ionosphere data reveal the coupling of neutral-ionized atmosphere [*Vadas and Crowley*, 2010; *Nishioka et al.*, 2013; *Azeem et al.*, 2015]. However, only *Vadas and Crowley* [2010] have shown their concentric waves in the ionosphere not to be associated primarily with tropospheric sources. Another study by *Smith et al.* [2013] models the presence of waves in images of the thermospheric red line emission as a product of a secondary wave generation somewhere below the peak of the layer. Recently, nightglow satellite imagery has allowed the detection of concentric gravity waves globally [*Akiya et al.*, 2014; *Gong et al.*, 2015; *Perwitasari et al.*, 2015; *Miller et al.*, 2015]. According to these reports, the sources of the observed concentric waves are again in the lower atmosphere and associated with deep convection, summertime midlatitude convection, wintertime extratropical jets, or island topography, as revealed in the survey by *Gong et al.* [2015].

In this paper, we report a ring-like wave event observed on 23 March 2012, in two different nightglow emissions over the Andes Lidar Observatory (ALO) (30.3°S, 70.7°W). In contrast to other accounts, we have strong evidence that convection did not generate this event at lower altitudes, but it was likely a product of a secondary wave generation by a point-like body force source at mesospheric heights, which makes this a unique register. Section 2 gives a complete quantitative description of the wave in images of two nightglow emissions, while section 3 presents the signature of the ring-like wave in other collocated instruments in our facility. Section 4 discusses the source location, and section 5 examines the potential point-like excitation mechanisms of the event. The summary of our findings is provided in section 6.

2. Characteristics of the Ring-Like Wave in Images of the OH and O(^1S) Nightglows

Figure 1 (Figure 2) presents the temporal and spatial evolution of the ring-like wave in a sequence of OH (O(^1S)) nightglow images. The images represent an uniform 512 × 512 km^2 grid of geographical coordinates, which the assumed altitudes for the OH and O(^1S) emissions are 87.8 km and 96 km, respectively. The integration time for images was 60 s for the OH and 90 s for the O(^{1}S). To enhance the contrast of high-frequency oscillations, we have utilized time difference filtering, which is accomplished by subtracting an image frame from the next [*Tang et al.*, 2003; *Vargas et al.*, 2009]. Technical issues in the ALO all-sky imager system caused the time gaps between some of the images in both Figures 1 and 2. The imager system operating at ALO has been described in detail in *Li* [2011].

Figure 1 presents the temporal and spatial evolution of the wave in OH emission only. The first image, taken at 07:07:58 UT, shows ring-like wavefronts arising in the eastern sector at about half distance from the zenith to the east edge of the frame. The image taken 9 min later (07:18:34 UT) shows three ridges of the packet. We observe four ridges in the frame recorded at 07:36:41 UT. The number of ridges increasing with time suggests that a coherent and active source was producing the oscillation. The Milky Way, which is brighter than the average pixel intensity due to the relatively wider bandwidth OH filter, eclipsed the wave prior to 07:03:00 UT (not shown) in the OH.

In the O(^1S) image sequence (Figure 2), the wavefronts emerged first at 07:03:56 UT. The O(^1S) image of the event at 07:33:29 UT exhibits a similar wave pattern of that in OH at about the same instant. Observe that the green line image is smoother than that in OH suggesting a higher buoyancy stability at the O(^1S) layer altitude. The last O(^1S) image of the event was taken at 08:20:00 UT (not shown). The event duration encompassed 01:20:00 h.

2.1. Observed Wave Parameters

Because the images are projected onto a regular grid of geographical coordinates with resolution of 1 km/pixel, a direct visual inference of the horizontal wavelength could be made. A horizontal wavelength $\lambda_h \sim 20\pm 2$ km was estimated in this way from the mean separation of successive wave peaks. We have assigned an uncertainty of 10% in this wavelength calculation.

We have also determined the horizontal wavelength λ_h from the two-dimensional fast Fourier transform (2DFFT) of the images. We applied the 2DFFT in a sequence of six images, which one of them is in Figure 3a. By this technique, we could also estimate the observed period, an the observed phase speed of the ring-like wave. For the parameters estimation, we have used a region of interest (ROI) of 135 × 175 km^2, highlighted by the white dashed box in the image and enlarged in Figure 3b (pixels within the box had intensity values multiplied by 10 to improve the contrast). The dashed box lies over the wave segment traveling about 75° with respect to the horizontal wind orientation (Figure 5). The 2DFFT was applied only in the ROI of each

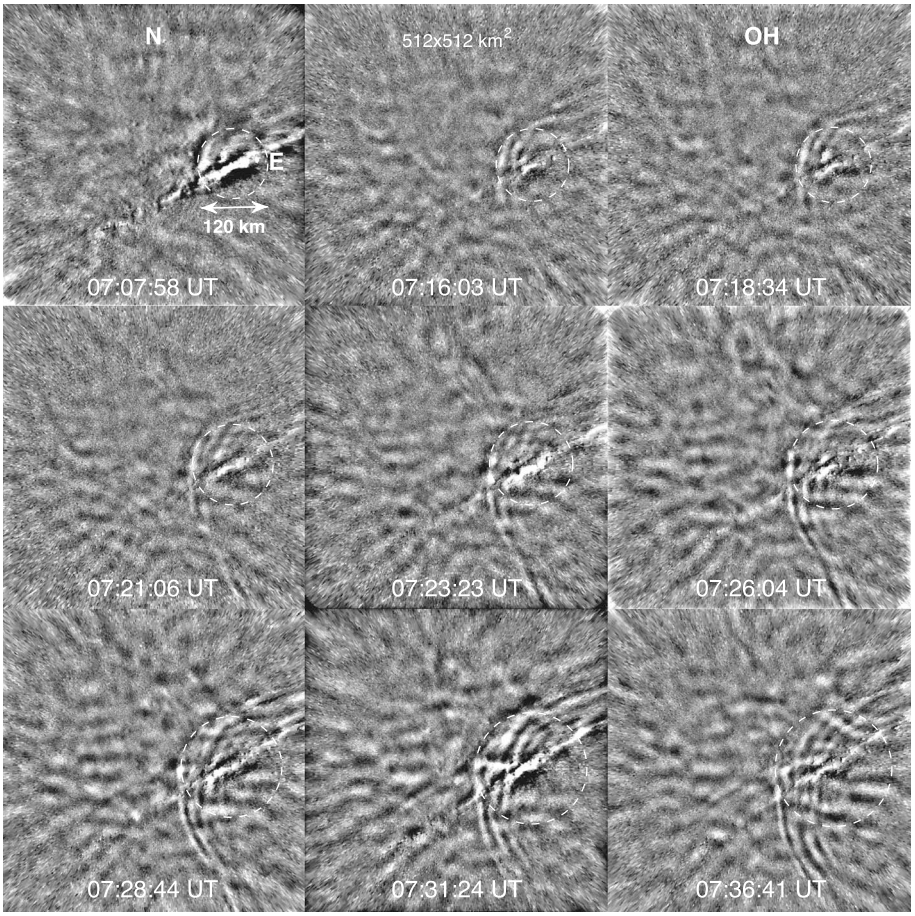

Figure 1. A sequence of time difference images of the OH nightglow showing the spatial and temporal evolution of the ring-like wave event observed at ALO during the night of 23 March 2012. The white dashed circles show the location of the leading wavefront in the field of view for a given instant.

intensity frame of the sequence. To isolate the spectral peaks of the 2DFFT associated with the ring-like wave, we have smoothed the images using a Butterworth filter with band pass in the 13–50 km horizontal wavelength range. Figure 3c shows the result of this filtering operation.

Figure 3d shows the ROI of four images and their respective spectrograms obtained from the 2DFFT decomposition. The central wavelength of the dominant peak corresponds to a wave of $\lambda_h \sim 19.7 \pm 2.0$ km, in good agreement with our visual determination of the horizontal wave scale. The uncertainty in λ_h from the spectral method is usually less than 10%. To calculate the horizontal wavelength, we obtain first the zonal (k_x) and the meridional (k_y) wave numbers from the peak of interest (black circles in the periodogram), then the horizontal wavelength by $\lambda_h = \frac{2\pi}{\sqrt{k_x^2+k_y^2}}$.

By tracking the phase of the spectral peaks with time, we have estimated the observed phase speed of the wave [e.g., *Garcia et al.*, 1997]. The bottom chart of Figure 3d shows the variation of the phase of the peaks with time, which are represented by the black circles. The time variation of the phase is given by the slope of the fitting curve of the points (solid line), which is −21.5 rad/h, and translates into an observed phase speed of $c_{\mathrm{oh}} = 18.8 \pm 1.9$ m/s. The observed wave period for the ring-like event is then $\tau_o = \lambda_h / c_{\mathrm{oh}} = 17.5 \pm 2.5$ min.

The observed horizontal phase velocity of the wave was also estimated by following the expansion rate of the ring-like wavefronts. To obtain the wavefronts expansion with time, we have fitted white dashed circles on top of the outermost ring of the wave in Figure 1 and then measured the diameter and the radius of the circle in each frame. The diameter of each circle is readily known as a full image frame covers an area of 512×512 km^2 and has a resolution of 1 km/pixel. Figure 4 shows explicitly how the radius of the wavefront changes with time (dark circles). The solid line is the best fit of the curve and has a slope of 26.0 ± 4.2 m/s that is just the

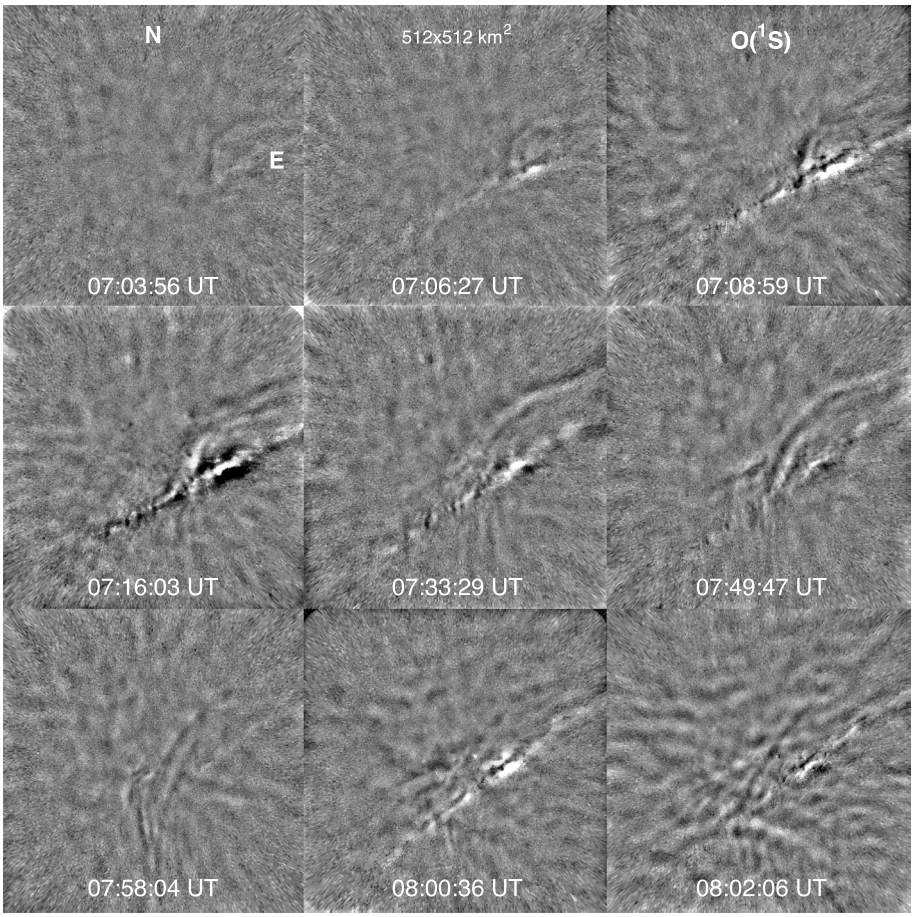

Figure 2. A sequence of time difference images of the O(^{1}S) nightglow showing the spatial and temporal evolution of the ring-like wave event observed at ALO during the night of 23 March 2012.

horizontal phase velocity the ring-like wave. By dividing the phase velocity by the horizontal wavelength, we obtain a wave period of $\tau_o = 12.6\pm 2.4$ min. The difference in the observed wave period obtained by these two methods resides in that the visual method evaluates the ring-like wavefronts as a single object, while the 2DFFT separates the distinct wave modes of the packet on the spectrogram once the wave is not entirely monochromatic. However, both period measurements are still consistent as they coincide at the extreme of 15 min.

2.2. Intrinsic Wave Parameters

Concurrent wind measurements provided by a meteor radar system (see the system description in *Franke et al.* [2005]) collocated at ALO allowed for the estimation of the intrinsic parameters of the ring-like event. Typically, the magnitude of the horizontal wind is assumed uniform across the 200×200 km^2 field of view of the meteor radar [*Hocking et al.*, 2001], but we have extrapolated that assumption to the 512×512 km^2 area of the image projected onto geographic coordinates.

Figure 5a shows a cross section of the magnitude of the horizontal wind from the meteor radar data in the range of 80–100 km. The arrows in Figure 5b show the orientation and the magnitude of the wind from 7–8 UT at ~ 87.8 km and ~ 96.0 km height, the averaged centroid altitude of the OH and O(^{1}S) layers, respectively. Although the horizontal wind in both layers is southeastward, its magnitude is larger at the green line layer altitude, reaching values of ~60 m/s there.

The background wind Doppler shifts the wave period and alters its intrinsic phase speed; we need to correct this effect prior using the GWs dynamic equations. The intrinsic wave period is calculated by the following:

$$\tau_i = \frac{\tau_o \lambda_h}{\lambda_h - \tau_o \bar{V} \cos \xi} \tag{1}$$

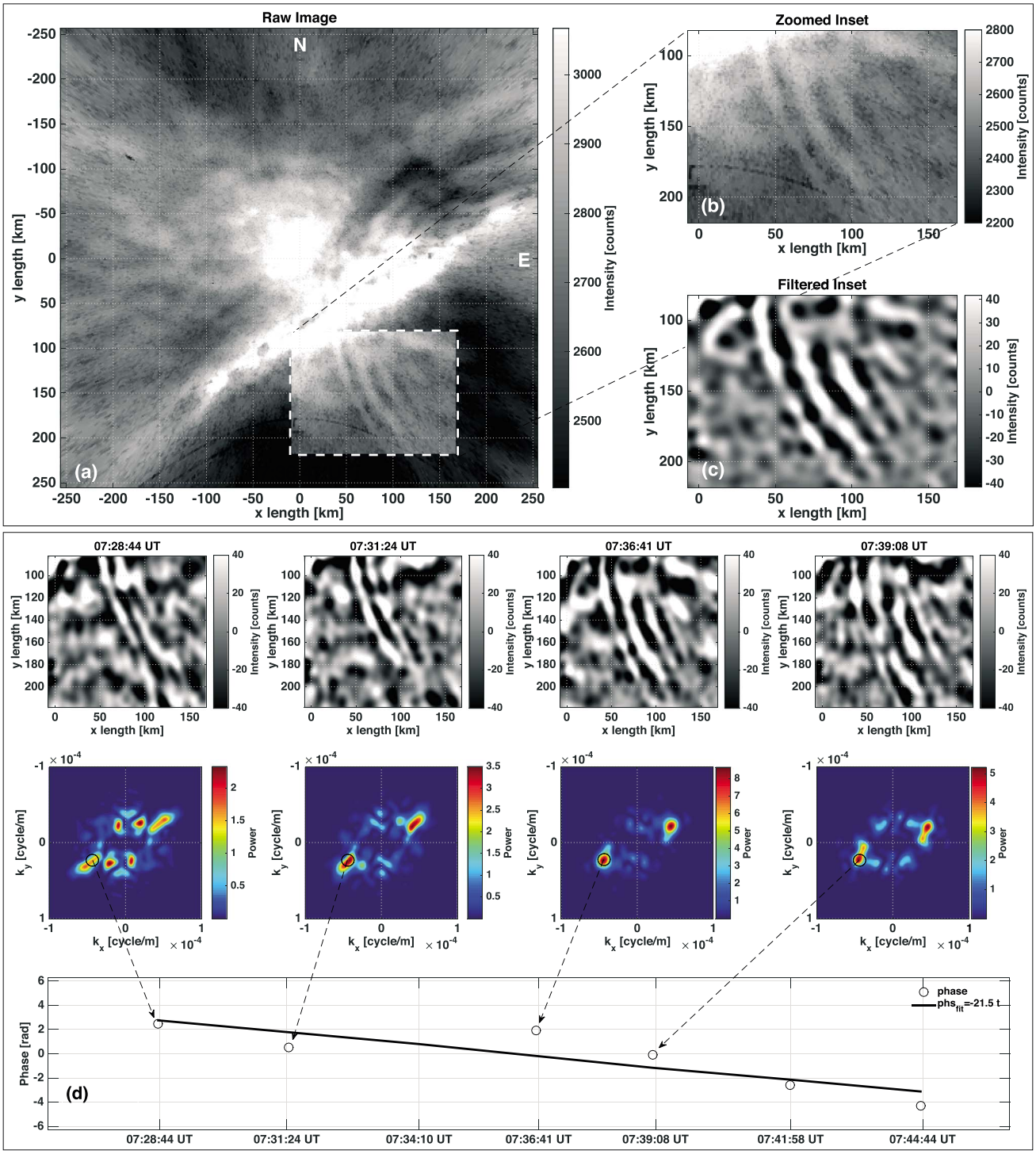

Figure 3. (a) Raw OH intensity image taken at 07:36:41 UT illustrating the ring-like wave on the southeast region of the FOV, (b) zoomed inset of the highlighted region, (c) inset of the highlighted region after a Butterworth filtering (cutoffs between 13 and 50 km), and (d) time variation of the phase of the dominant spectral peak in the 2DFFT of each image of the sequence (highlighted region). The dominant spectral peak correspond to $\lambda_h = 19.7 \pm 2.0$ km. The slope of the fitting curve (solid line) translates in an observed phase speed $c_{oh} = 18.8 \pm 1.9$ m/s.

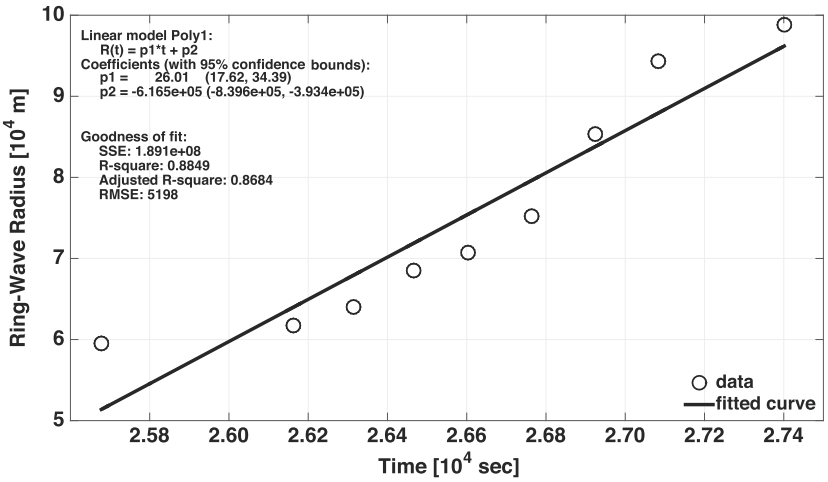

Figure 4. Expansion of the ring-like wave radius with time. The markers are the radius of the wave represented by the dashed white circles in each frame of Figure 1. The slope of the fitting curve (dashed red line) gives an estimated horizontal phase velocity of the wave as ~26± 4.2 m/s. The horizontal axis values correspond to the time in seconds elapsed since 00:00 UT on 23 March 2012.

where τ_o is the apparent period, λ_h is the horizontal wavelength, and $\bar{V} = \sqrt{u^2 + v^2}$ is the background wind magnitude (u = zonal wind component and v = meridional wind component). Also, ξ is the angle between the background wind and the horizontal wave number vector.

Equation (1) illustrates how the intrinsic period changes as ξ increases. Figure 6 shows explicitly the τ_i variation for $\tau_o = 17.5$ min and $\lambda_h = 19.7$ km (the ring-like wave dynamic parameters), and $\bar{V} = 32$ m/s (the background wind magnitude at the OH layer). For instance, when $\xi = 180°$, the wave travels directly into the background wind, and $\tau_i = 6.5$ min, corresponding to the shortest intrinsic period (the largest intrinsic phase speed). As the angle ξ deviates from 180°, the intrinsic period increases accordingly (the wave slows down). At $\xi = 90°$, $\tau_i = \tau_o$, and $c_{ih} = c_{oh}$. For $\xi \leq\sim 60°$ or $\xi \geq\sim 300°$, the intrinsic period becomes negative, indicating that the magnitude of background wind component toward the wave direction becomes larger than the wave phase speed, which creates a barrier where the wave is no longer propagating. The altitude where the intrinsic phase speed $c_{ih} = c_{oh} - \bar{V}\cos\xi = 0$ is known as a critical level [*Fritts et al.*, 2006].

The distinct wave segments will have different intrinsic parameters because the ring-like wave is horizontally asymmetric. The ring-like wave segment highlighted in Figure 3b makes an angle of 75° respect to the background wind (or $\xi = 105°$) and has an intrinsic period $\tau_i = 12.1\pm 1.9$ min. As the horizontal wavelength does not change very much in the highlighted ROI, the intrinsic horizontal phase speed of that wave segment is then $c_{ih} = \lambda_h/\tau_i = 27.1$ m/s. The black circles in Figure 6 represent the intrinsic parameters of the wave segment showed in Figure 3b.

To understand how curved wavefronts become planar as the wave expands, consider that different wave segments are affected differently by the wind because their distinct orientations. Assuming that the horizontal wind is uniform across the area covered by the wave, notice that each wave segment will make a different angle respect to the background wind. Thus, the magnitude of the wind will be different for each of the wave segments. These segments will then oscillate at different intrinsic periods due to this, although their apparent phase speeds are invariant. Consequently, the wave structure will change as it propagates horizontally due to this nonuniform interaction with the background wind.

2.3. The Vertical Wavelength and Vertical Group Velocity

The vertical wavelength is usually estimated implicitly from the gravity wave dispersion relation as long as the intrinsic parameters are known. The dispersion relation is given by [*Hines*, 1960]

$$m^2 = \frac{N^2 - \omega^2}{\omega^2 - f^2}k_h^2 + \frac{\omega^2}{\gamma g H} - \frac{1}{4H^2} \tag{2}$$

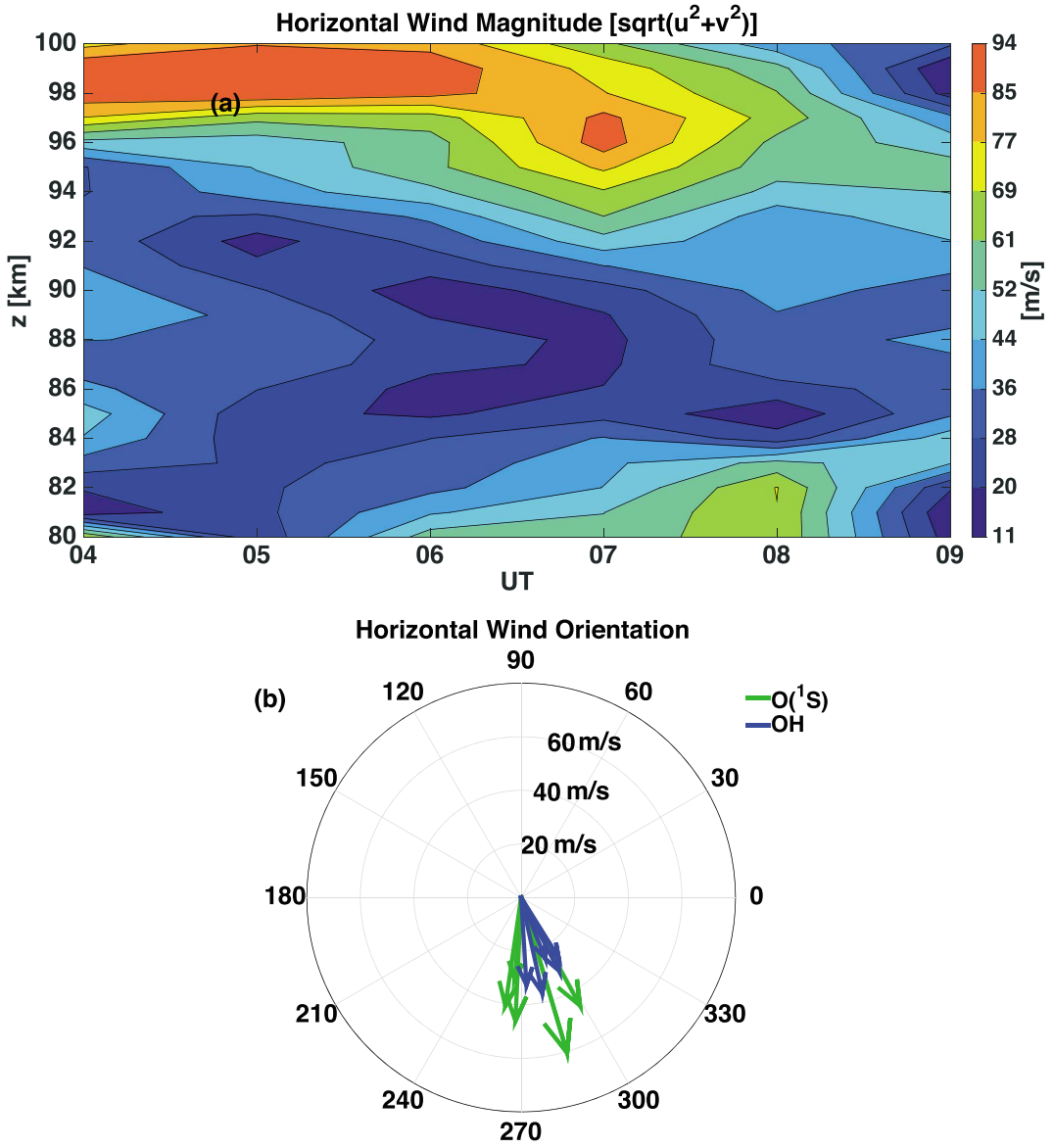

Figure 5. (a) Cross section of the horizontal wind magnitude measured by the ALO meteor radar system and (b) horizontal wind orientation at the peak of the OH and O(^{1}S) layers. The horizontal wind at the OH and O(^{1}S) was obtained assuming the layer centroid at 87.8 and 96 km, respectively.

where $m = 2\pi/\lambda_z$, $\omega = 2\pi/\tau_i$, and $k_h = 2\pi/\lambda_h$ are the vertical wave number, intrinsic frequency, and horizontal wave number, respectively; $\gamma = 1.4$ is the ratio of specific heats, $g = 9.5$ m/s^2 is the gravity acceleration, N is the Brunt-Väisälä frequency, H is the scale height, and f is the inertial frequency. From our lidar data obtained during the ring-like event we have $N = 0.017$ rad/s and $H = 7$ km, and have assumed $f = 7.3 \times 10^{-5}$ rad/s. Using the intrinsic parameters calculated previously for the ring-like wave, we obtain the vertical wavelength $\lambda_z = 2\pi/m = 11.2 \pm 2.8$ km.

The vertical group velocity of our wave is derived from the linear gravity wave theory [*Hines*, 1960]. It is given by the following:

$$c_{gz} = \frac{\partial \omega}{\partial m} = -\frac{m}{\omega} \frac{\omega^2 - f^2}{m^2 + k_h^2 + 1/4H^2}. \quad (3)$$

Plugging in equation (3) reasonable values for each constant and using the intrinsic wave parameters, we have estimated $c_{gz} = 11.6 \pm 4.6$ m/s.

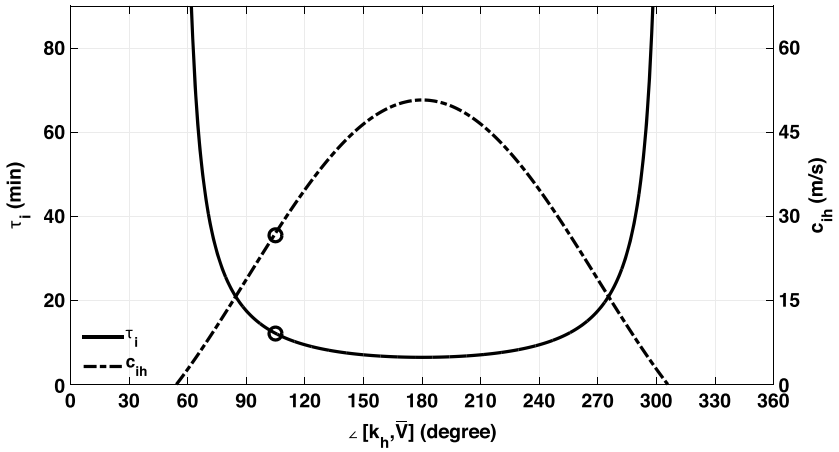

Figure 6. Intrinsic wave period (solid line) and intrinsic horizontal phase speed (dashed line) respective to the horizontal wind vector orientation at the altitude of the OH layer considering the background wind velocity $\bar{V}$ = 32 m/s. The black circles correspond to the intrinsic parameters for the wave segment highlighted in Figure 3.

3. The Signature of the Ring-Like Wave in TMapper and Lidar Data

The mesosphere temperature mapper (TMapper) simultaneously records the OH intensity and rotational temperature during the night [*Pendleton et al.*, 2000; *Taylor et al.*, 2001]. Figure 7 shows the time variation of both intensity and rotational temperature of the OH nightglow given by the TMapper data during the night of the ring-like wave event corresponding to pixel values located at the center of each image only. The TMapper image size is 128 × 128 pixels because they are heavily binned (8 × 8) to improve the signal-to-noise ratio. A complete discussion of the TMapper can be found in *Taylor et al.* [2001]. Notice the large oscillation caused by the ring-like wave from 7:30–8:30 UT in the OH intensity (solid line), more than ∼11.5% of the mean. The rotational temperature (dotted line) changes by about 4% of the mean during the same time span.

The lidar temperature and Na density fluctuations around the occurrence time of the ring-like wave are in Figure 8 (see the lidar description in *Franke et al.* [2005]). From 7.2 UT to 7.8 UT we have measured temperature changes of 15–20% in the 84–88 km altitude range (Figure 8a) and a temperature peak of 230–241 K just below 86 km altitude at 7.2 UT. On the other hand, the Na density fluctuates by ∼150% at 84–88 km due to the ring-like wave oscillation (Figure 8b) and shows a peak of 3682–4051 atoms/cm^3 just above 85 km at ∼8 UT. The density enhancement is likely caused by the Na downward transport due the ring-like wave that changes the vertical wind abruptly and causes the convergence of Na atoms toward the altitude where the vertical wind perturbation peaks. The relative wave fluctuations in both temperature and Na density were obtained as follow: a linear fit was first calculated for each altitude of the measured temperature and Na density fields to obtain their nonperturbed backgrounds, and these background fields were then subtracted from

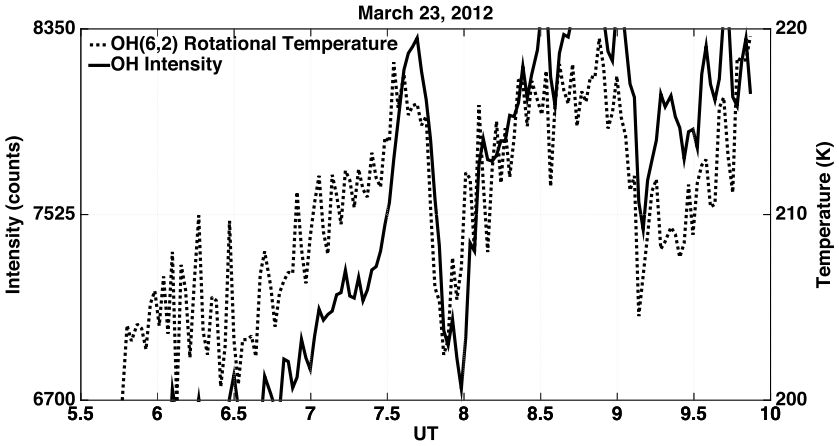

Figure 7. Mesosphere Temperature Mapper measurements of the OH intensity and rotational temperature.

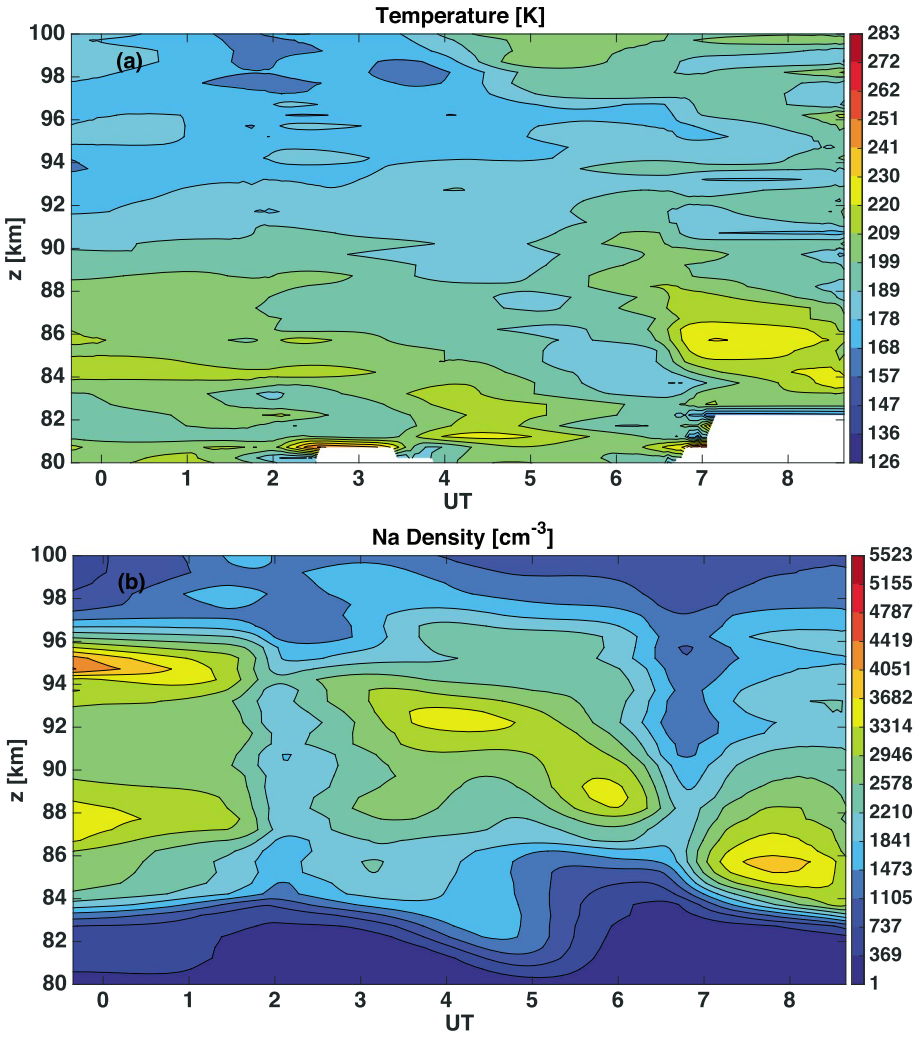

Figure 8. Lidar measurements of (a) ambient temperature and (b) Na density during the occurrence time of the ring-like wave.

the measured temperature and Na density to isolate the wave fluctuation, respectively. More details of this method is given in *Gardner and Liu* [2007].

When the lidar temperature and the Na density are filtered in the time domain for a wave of 17.5 min observed period, the absolute wave amplitude in temperature and Na density is ~5 K and 250 cm^{-3}, respectively. The lidar temperature response to the ring-like wave is relatively larger than that in the rotational temperature because the TMapper observes the integrated column of the nightglow intensity. The integrated nightglow column has a limited response for waves presenting vertical wave scale smaller than the layer thickness [*Vargas et al.*, 2007].

We have inferred the vertical wavelength of the ring-like wave event from the ratio between the fluctuation in TMapper nightglow intensity (I') and that in the lidar temperature (T'). To do that, we have also used the cancellation factor (CF) model proposed by *Swenson and Gardner* [1998], *Liu and Swenson* [2003], and *Vargas et al.* [2007]. The cancelation factor is the ratio of the relative nightglow intensity (measured by the TMapper) to the ambient temperature (measured by the lidar) and depends critically on the vertical scale of the gravity waves. By calculating the ratio I'/T' and comparing it to the model [*Vargas et al.*, 2007, Figure 5], we could infer the vertical wavelength of the wave independently of the dispersion relation. Thus, the cancelation factor obtained from the TMapper intensity versus lidar temperature ratio is CF = 1.5 and is associated with a wave of $\lambda_z \sim 15$ km (a freely propagating wave). This vertical wave scale is consistent with that obtained previously

using the dispersion relation (equation (2)), but the discrepancy could be due to the larger uncertainties in the temperature measured at the bottom of the Na layer.

4. The Source Location

Many wave sources are active throughout the atmosphere and different physical mechanisms associate with them. Studying the spatial and temporal characteristics of the wave source is essential to determine which mechanism is exciting the waves. The reverse ray tracing of observed GWs is a necessary tool to locate the wave source when background wind data are available [*Vadas and Fritts*, 2004]. Using a simplified ray tracing scheme, we have calculated here the vertical position of the wave source assuming a quasi-stationary source position within the imager field of view (FOV).

To estimate the source's altitude, we have first studied the horizontal expansion of the leading wave-front with time. The time it takes to expand horizontally from its center position to a distance r is roughly the same it takes to travel vertically from the source up to the OH layer centroid $z_{OH} \sim 87.8\pm 2.5$ km height, where the uncertainty in the layer centroid is estimated in *Zhao et al.* [2005]. The traveling time t_r is then the radius of the leading wavefront at a given instant divided by the wave's observed phase speed.

Figure 1 shows the outermost wavefront of 60 ± 2.5 km radius registered in the OH image taken at 07:07:58 UT, where the uncertainty in the radius was estimated from the assigned uncertainty in the wavefront diameter ($\sigma_D \sim \frac{\lambda_h}{4}$). The radius of the wavefront was estimated from the fitting circle as the projected image area is 512×512 km^2. As $c_{oh} = 18.8\pm 1.9$ m/s, the traveling time the leading front takes to expand horizontally from $r=0$ (the source) to $r=60$ km is $t_r = r/c_{oh} = 53.2\pm 5.8$ min. Notice that we have assumed a horizontal wind of zero magnitude here; thus, the wave parameters are unchanged in the altitude range. In this way, the source height must be located at $z_s = z_{OH} - c_{gz}t_r \sim 52\pm 15$ km, where $c_{gz} = 11.6\pm 4.6$ m/s is the vertical group velocity of the ring-like wave obtained from equation (3). A wave source located at 52 ± 15 km suggests a nontropospheric excitation in the upper stratosphere-mesosphere altitude range (from 37 to 89 km).

We have also carried out the reverse ray tracing of the event to verify the location of the source against the previous estimation. The available temperature and horizontal wind data provided by the lidar and the meteor radar were used as inputs in the reverse ray tracing model.

Figure 9 shows the result of the reverse ray tracing calculations. Figures 9a and 9b are, respectively, the 2-hours averaged atmospheric temperature in the time span of the ring-like event and the horizontal wind components u (zonal) and v (meridional). The magnitude of the wind shear in both zonal and meridional directions is less than 10 m/s/km, and the temperature gradient is larger than −7 K/km in the range; thus, the region is dynamically and convectively stable. Figure 9c shows that $N > 0$ in the range (solid line), while the ring-like wave intrinsic frequency (dash-dotted line) is positive up to ∼92 km. Figure 9d shows that $m^2 > 0$ in the mesospheric range; thus, the ring-like wave is vertically propagating, but larger m^2 values in the 90 to 94 km implies a shorter vertical wavelengths and wave absorption conditions there (critical level). Figure 9e demonstrates that the ring-like wave vertical group velocity is small below 92 km but gets larger above that level, while the horizontal group velocity c_{gh} is larger below 92 km but becomes negative above 92 km.

Figure 9f presents the x-z path traveled by the wave given the atmospheric conditions for the night in the mesosphere/lower thermosphere (MLT). The initial altitude of the wave trajectory is set at about the OH layer centroid. Because the magnitude of the vertical group velocity of the wave is small, the distance traveled is short (∼10 km). Horizontally, the group velocity is $c_{gh} <\sim 10$ m/s between 80 and 90 km, and the horizontal distance traveled is ∼65 km in the range. This traveled horizontal distance is comparable to the radius of the wave observed in the OH image of 07:07:58 UT, which suggests that the source location must be close to the 80 km level and likely in the lower MLT region (60–80 km).

Because the lack of wind measurements below 80 km, we have carried out the ray tracing in the 90 to 80 km range only. However, we present in Figure 10a Sounding of the Atmosphere using Broadband Emission Radiometry (SABER) temperature profile taken at 4:35:44 UT about 1000 km away from ALO at (31.2°S, 81°W) geographical coordinates. The static stability in Figure 10b calculated from Figure 10a shows $N^2 < 0$ at 80–85 km range, where the conditions for the vertical propagation of the ring-like wave would not be ideal. However, the 1-hour averaged temperature profile from our lidar system plotted as the red continuous curves on top of the SABER profile indicates that the region above ALO would be convectively stable, and the ring-like wave would be vertically propagating in the region.

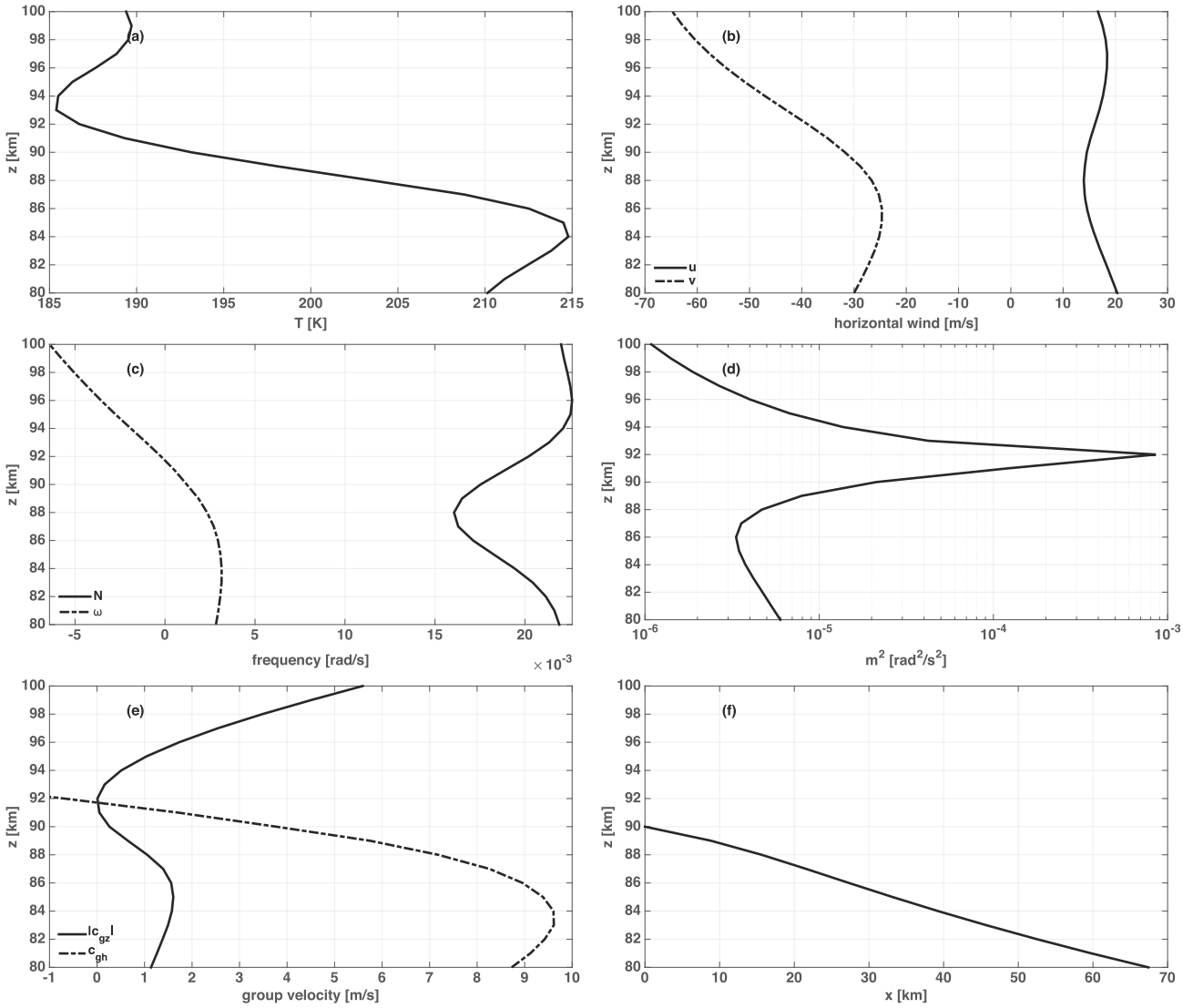

Figure 9. The reverse ray tracing calculation for the ring-like wave. (a) The 2 h averaged temperature as measured by the ALO lidar system; (b) zonal (solid line) and meridional (dash-dotted line) wind provided by the ALO meteor radar; (c) Brunt-Väisälä frequency (solid line) and wave frequency (dash-dotted line), and (d) the squared vertical wave number. (e) The vertical (solid line) and horizontal (dash-dotted line) group velocity of the ring-like wave, and (f) the *x*-*z* path of the ring-wave for the atmospheric conditions of the night.

5. The Excitation Mechanisms of the Ring-Like Wave

Some physical mechanisms would excite waves in higher altitudes, but we must rule out tropospheric sources first to then find the most likely excitation mechanism above the tropopause. The meteorological conditions at ALO during the ring-like wave event are presented in Figure 11. The Geostationary Operational Environmental (GOES 13) and the Lightning Imaging Sensor (LIS) satellites have recorded images of the cloud coverage (Figure 11a) and the lighting activity (Figure 11b) around the ALO region, respectively. The red squares in each panel represent the area of the nightglow images mapped onto geographic coordinates. It is evident in Figure 11a the absence of convective plumes around ALO on 23 March 2012 at 07:00 UT, and earlier images also show no evidence of deep convection around the observation site. The lightning activity in the region is also small, as noticed in Figure 11b that shows the lightning activity for the whole month. The presence of lightning strokes is more intense in the southeast sector of the image but still far from the area covered by the ALO nightglow imager. In fact, during the day of the ring-like wave event no lightning event was detected around the ALO region. Recognizing that lightning activity and cloud coverage are proxies of deep convective

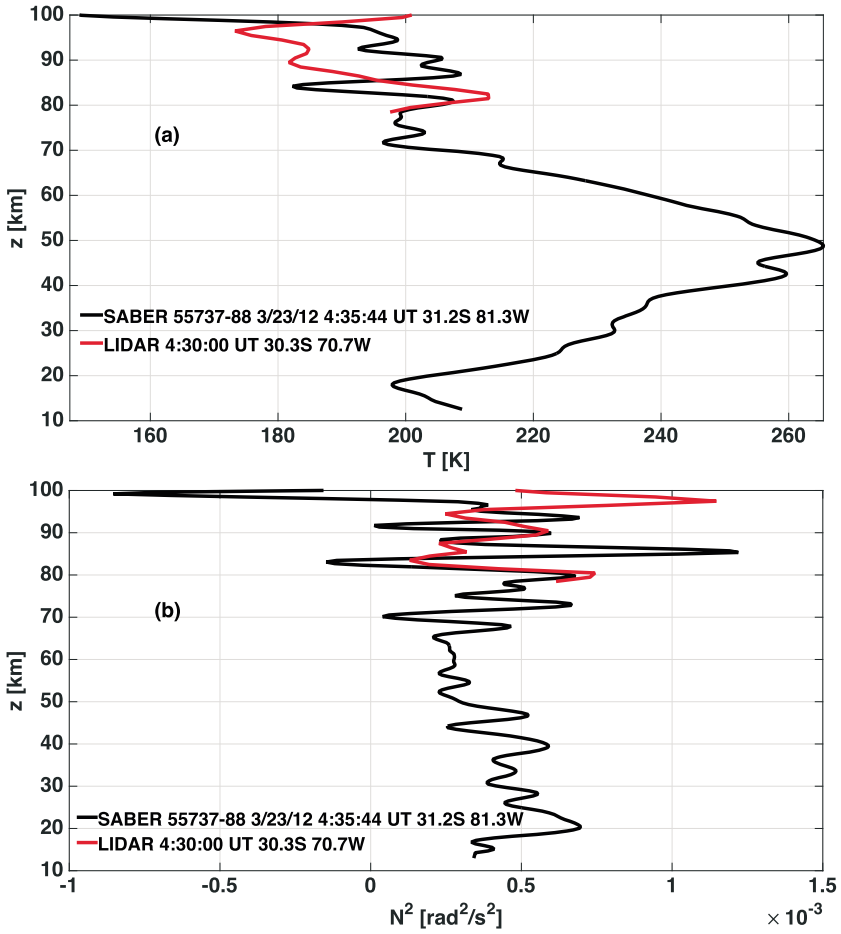

Figure 10. The (a) thermal structure and (b) static stability of the mesospheric region near ALO observed by the SABER satellite (orbit 55737 event 88) and the ALO lidar system around 4:30:00 UT on 23 March 2012. Notice that the SABER profile was taken ~ 11° longitude west of ALO (~1000 km away).

activity, and because deep convection is an active source of high-frequency GWs, it is unlikely that a tropospheric source near to the ALO region would have directly triggered the ring-like wave reported here.

Another active source of gravity waves at the lower levels is the incidence of horizontal winds on high mountain chains. The ALO region surrounding topography is marked by the Andes Cordillera, where the production of orographic gravity waves must be high. Nevertheless, orographic sources excite essentially low-frequency oscillations and could not cause the ring-like wave reported here, which is a high-frequency oscillation. Therefore, we also rule out the Andes orography as the source of the ring-like wave.

As tropospheric generation mechanisms are ruled out, the source location must be then far from convective levels and feasible excitation mechanisms at higher altitudes must be invoked. For instance, the body forcing due to breaking gravity waves is a source mechanism that has taken the modelers attention during the past decade [*Zhu and Holton*, 1987; *Vadas and Fritts*, 2001, 2002, *Snively and Pasko*, 2003; *Vadas et al.*, 2003; *Smith et al.*, 2013]. This mechanism would trigger waves at any atmosphere level where wave breaking occurs.

Vadas and Fritts [2002] represent the body forcing in terms of a GW flux divergence parameterization, which yields a double effect at the forcing location. First, the body forcing accelerates the mean flow due to the gravity wave drag; second, the body forcing excites secondary waves in spatial/temporal scales associated with the forcing geometry and frequency. Besides, the body forcing can excite GWs in two manners: (1) via the radiation of GWs at higher harmonics of the primary wave [*Vadas et al.*, 2003] and (2) via geostrophic adjustment of disturbed vorticity/temperature fields at the breaking location [*Zhu and Holton*, 1987].

The geostrophic adjustment may excite gravity waves at any altitude where the unbalanced flow takes place. *Zhu and Holton* [1987] have shown in a 3-D model the radiation of waves from a forcing region. In this region,

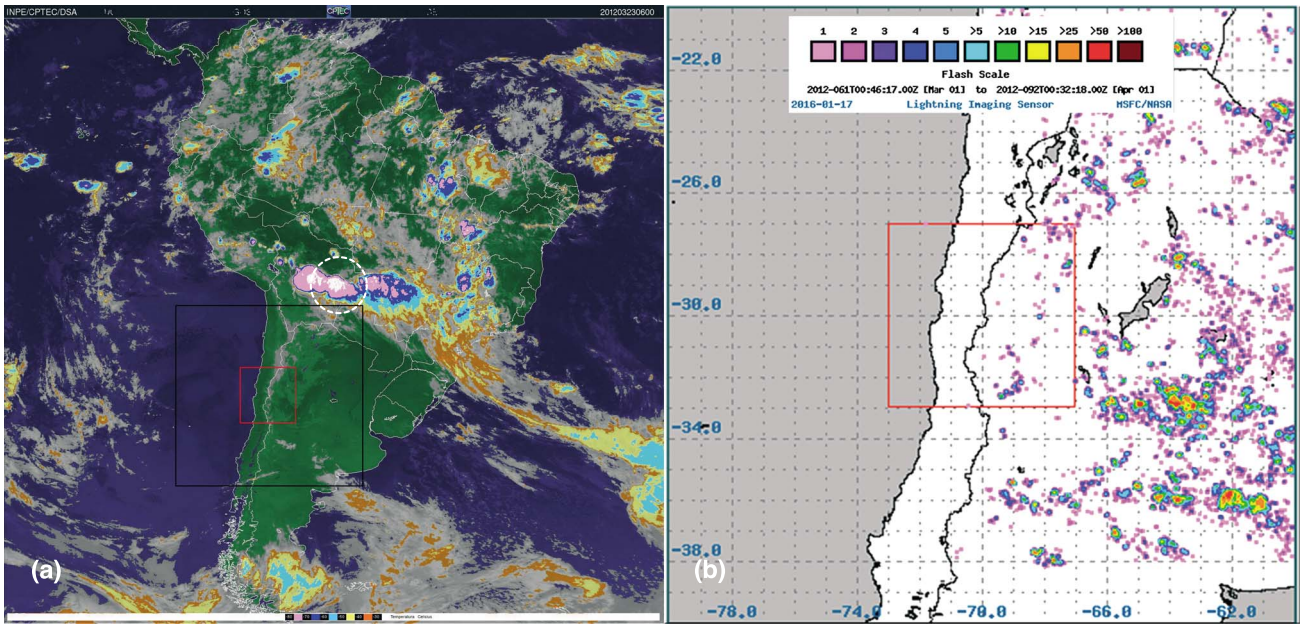

Figure 11. (a) The cloud cover and cloud top temperature over the South America sector registered by the GOES 13 satellite on 23 March 2012 at 07:00 UT and (b) the lighting activity near the Andes Lidar Observatory region for 23 March 2012 by the Marshall Space Flight Center/LIS satellite. The black square in Figure 11a corresponds to the full area in Figure 11b. The red squares in each frame represent the area covered by OH nightglow images projected onto the geographical coordinates of the site. The white dashed circle encloses the source region of the primary wave located ~1400 km from ALO.

the geostrophic adjustment process occurred because of the breaking of parent gravity waves. Although the wave spectrum generated by the adjustment process presents relatively large amplitudes in their simulations, the frequency of excited waves is near the inertial, low-frequency regime. Once the event reported here is in the high-frequency wave regime, we conclude that the geostrophic adjustment process is an unlikely source of the ring-like wave.

The secondary wave generation, still in a theoretical framework, excites a wave spectrum of similar characteristics of our ring-like wave. *Vadas and Fritts* [2001] and *Vadas et al.* [2003] modeled this process and showed that higher harmonic secondary waves are propagated from the region where a primary, larger temporal, or spatial scale wave breaks. Likewise, *Snively and Pasko* [2003] simulated the breaking of a 10 min period primary wave generated by squall line forcing at the tropopause. The ascending wave propagated onto the breaking altitude near the mesopause where a 5 min secondary wave emerged subsequently, characterizing a higher harmonic excitation. Thus, the high-frequency, ring-like wave reported here supports a scenario of a secondary wave excitation at mesospheric altitudes. A difficulty of this hypothesis is, however, that the primary wave is also in the high-frequency range and should be excited by a high-frequency source as well.

In order identify the primary wave that caused our ring-like wave, we observe first in Figure 11a the existence of a deep convection region over central Bolivia about ~1400 km northeast of ALO. The area of the primary wave source is enclosed by the white dashed circle and shows cloud top temperatures of about −80°C. Airglow images of the OH emission for the night clearly show larger horizontal scale waves traveling from northeast to southwest over ALO, which substantiates our hypotheses of a primary wave coming from the deep convection region indicated in Figure 11a. SABER satellite and Modern-Era Retrospective Analysis for Research and Applications (MERRA) model data were used to obtain, respectively, temperature and horizontal winds profiles near the deep convection source over Bolivia around (20.4°S, 52.6°W) geographical coordinates. These profiles were then used to study the trajectory of a hypothetical primary wave from its source over Bolivia down to the ALO area.

The trajectory of the primary wave was obtained from the forward ray tracing (Figure 12). A temperature profile for the deep convection region over Bolivia (Figure 12a) was taken from SABER satellite orbit 55,736 events 93 measured at 03:01:53 UT. The zonal and meridional wind profiles in Figure 12b were obtained from the MERRA model for the exact location of the deep convection center over Bolivia and averaged from 00:00:00 UT to 06:00:00 UT. The dynamic parameters of the primary wave were inferred from the ring-like wave (the

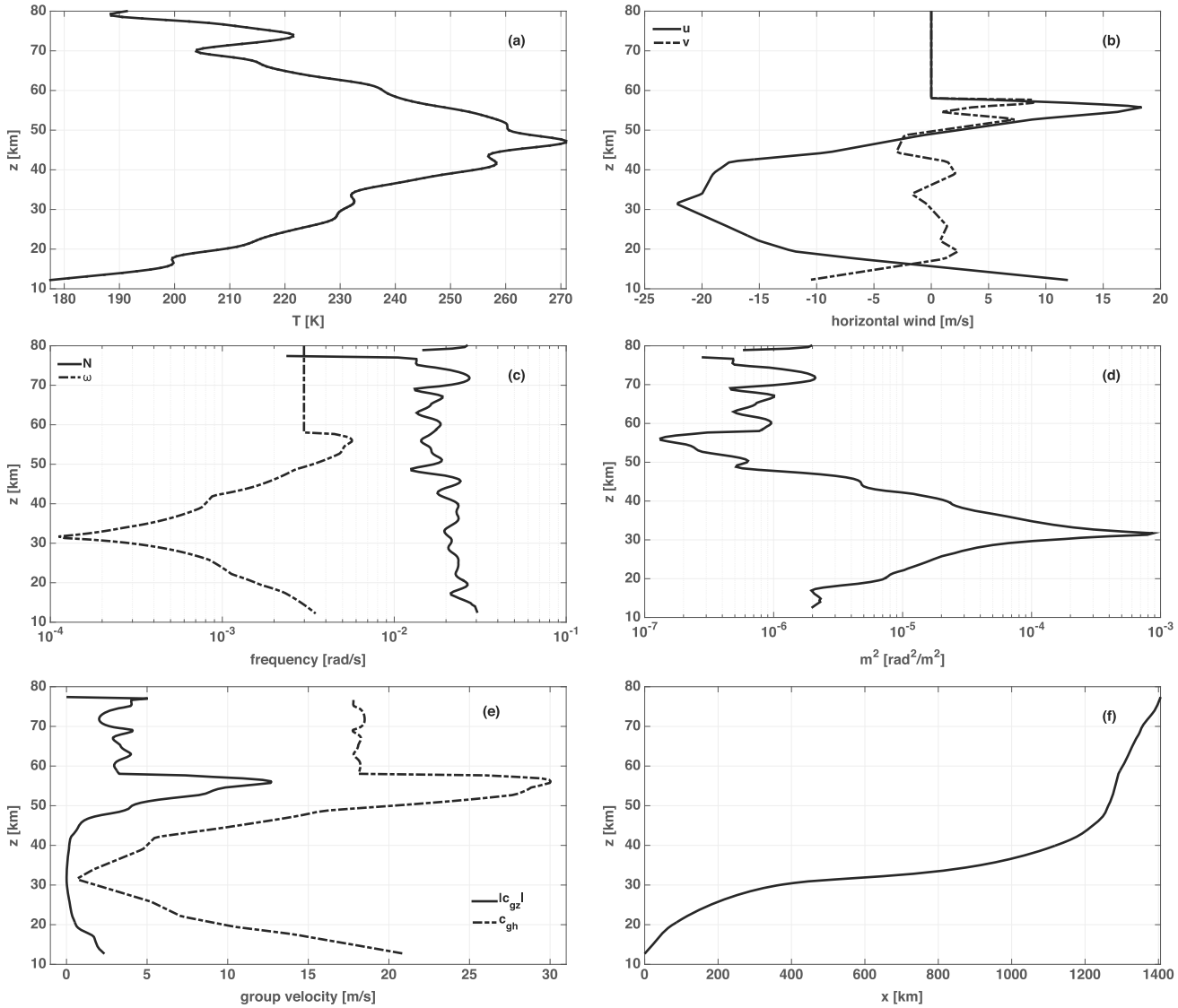

Figure 12. Forward ray tracing of the primary wave originated ~1400 km from ALO over Bolivia region (20.4°S, 56.2°W). (a) SABER satellite temperature (event number 93, orbit number 55736, 03:01:53 UT); (b) instantaneous 3-hourly 1.25° zonal and meridional winds (MERRA model MAI3CPASM v5.2.0); (c) altitude variation of the Brunt-Väisälä frequency and the primary wave frequency due to nonisothermic and nonstatic atmospheric structure (notice the critical level between 75 to 80 km altitude); (d) primary wave squared vertical wave number and (e) the vertical and horizontal group velocity. (f) Primary wave *x*-*z* trajectory from its source in the lower atmosphere to the critical level observed at 80 km altitude. Notice that the MERRA model provides winds up to 60 km only; we have assumed $u(z) = v(z) = 0$ m/s above that level.

secondary wave), assuming that the energy of the primary wave was transferred harmonically to the secondary wave having wave number and frequency of $\sim 2k$ and $\sim 2\omega$ [*Franke and Robinson*, 1999; *Snively and Pasko*, 2003], where k and ω are the wave number and the frequency of the primary wave, respectively. Thus, our secondary ring-like wave of λ_h =19.7 km and τ_o =17.5 min would imply in a primary wave of λ_h =39.4 km and τ_o =35 min. These are the dynamic parameters used to trace the trajectory of the primary wave from the source to the ALO region.

The static stability of the source region of the primary wave (Figure 12c) calculated from the SABER temperature demonstrates that the atmosphere is convectively stable in the 10 to 75 km range and presents a critical level from ~75 km to ~80 km where $N^2 < 0$ because the environmental lapse rate is smaller than −9.8 K/km. The intrinsic primary wave frequency also in Figure 12c (dash-dotted line) is less than N in the range and reaches smaller values at ~30 km due to the Doppler shift caused by the background wind on the intrinsic primary wave frequency. Because the MERRA model only provides horizontal wind data up to 60 km, we have

set $u(z) = v(z) = 0$ m/s above that range where the wave frequency becomes constant. The square of the vertical wave number in Figure 12d is positive in the range (the wave is vertically propagating) but assumes larger values at 30 km as well, where the vertical wavelength gets small, indicating the wave has come close to an absorption level. Observe this effect on the vertical group velocity (Figure 12e), which tends to zero near 30 km level, demonstrating that the wave has slowed down.

The *x-z* trajectory is finally displayed in Figure 12e, which reveals the primary wave would travel horizontally ~1400 km southwestward under the specified atmospheric conditions. The wave would take a long time in the 30 to 40 km range due to the small vertical and horizontal phase velocity in the region but would reach the 80 km level shortly after leaving that particular altitude range. Notice that the vertical propagation conditions are caused solely by the dynamic conditions depicted by the MERRA model winds for the night. Thus, under the specified conditions, we conclude that it would be feasible for a primary wave, excited by deep convection over Bolivia, to travel all way down to the ALO region, break or dissipate at 75–80 km due to a convectively unstable atmosphere, and then excite the ring-like wave reported here.

The nightglow images of the ring-like wave and the model of *Vadas and Fritts* [2001] permit to understand some spatial characteristics of the ring-like wave source. For example, the 07:07:58 UT image shows a wavefront confined in a 50×50 km^2 region. Earlier images show that the wavefront comprises an even smaller area, suggesting that the excitation happens in a highly localized, point-like source area. *Vadas and Fritts* [2001] have modeled the source of secondary waves as a spatial Gaussian body forcing caused by a primary breaking wave. The vertical (horizontal) full width at half maximum (FWHM) of the Gaussian is just σ_z (σ_x). The vertical wavelength is associated with the source depth by $\lambda_z \sim 2\sigma_z$, while the horizontal source extent is associated with the wave horizontal scale by $\sigma_x = 2\lambda_h$. We obtain from these relations $\sigma_z \sim 5.6$ km as $\lambda_z = 11.2$ km, and $\sigma_x \sim 39.4$ km as $\lambda_h = 19.7$ km. Notice that the horizontal extent of the body force is comparable with the horizontal wavelength of the primary wave discussed earlier in this section.

In sum, despite that the fact concentric waves have low occurrence rate, the secondary wave generation mechanism is supposed to occur continually throughout the middle atmosphere. However, after many years observing the mesospheric nightglow layers in Brazil (from 1998 to 2005) and Chile (from 2010 to 2015), we have only captured one single event of a ring-like wave within the field of view of our imagers or within a relatively small distance from the observation site for the wavefronts still be curved. Similarly, M. J. Taylor (private communication, 2012) has observed only one similar wave event within the FOV of his imagers. Because of this observational evidence, the secondary wave mechanism must be less dominant than thought as a source of GWs in the MLT according to the data available so far.

6. Summary/Conclusion

We have presented here a ring-like wave pattern observed in two nightglow emissions at ALO, Chile, on 23 March 2012. The dynamic parameters of the event, inferred from image processing, reveal a high-frequency wave with apparent period, phase speed, and horizontal wavelength of 17.5 ± 2.5 min, 18.8 ± 1.9 m/s, and 19.7 ± 2.0 km, respectively. Utilizing collocated meteor radar wind measurements, we have inferred an intrinsic period of 12.1 ± 2.5 min, intrinsic horizontal phase speed of 32.0 m/s, and vertical group velocity of 18.7 m/s for the ring-like wave. We have also estimated a vertical wavelength of 11.2 ± 1.9 km for the wave segment traveling 75° respect to the background flow utilizing the dispersion relation of GWs.

Images of lightning and cloud coverage from LIS and GOES satellites showed no evidence of convective plumes around the ALO region on 23 March 2012, suggesting that the source of the ring-like wave was not directly tropospheric. Also, the wave source has been located at 52 ± 15 km in the upper stratosphere-mesosphere range, which reinforces our assumption of a nontropospheric generation of the event. A more sophisticated reverse ray tracing scheme suggests that the wave source must be lower than the 80 km level. Among all the feasible sources, the ring-like wave is likely a product of a secondary wave excitation (body forcing due to a breaking primary wave). This secondary wave mechanism would radiate essentially high-frequency waves, in agreement with the frequency range of the ring-like event reported here. The source of the ring-like wave was probably the breaking or dissipation of a primary wave generated by deep convection in the troposphere over central Bolivia and about ~1400 km northeast of ALO, as reveled by the forward ray tracing of the primary wave.

We have noticed a very low occurrence rate of concentric, ring-like waves in imager registers. Because of that, the secondary wave excitation mechanism, which relates ultimately to the body forcing caused by breaking gravity waves, must be less dominant than proposed. We recognize that secondary wave excitation is an important source of GWs, but further observations will establish its significance related to other GW sources throughout the middle atmosphere.

Acknowledgments
This work was supported by the NSF grant 1136208 ("Collaborative Research: A Consortium of Resonance and Rayleigh Lidars"). The authors are grateful to the anonymous reviewers for their helpful comments. Andes Lidar Observatory data are available upon email request to the first author. MERRA data were obtained from the Global Modeling and Assimilation Office (GMAO) at NASA Goddard Space Flight Center through the NASA GES DISC online archive (http://disc.sci.gsfc.nasa.gov/daac-bin/DataHoldings.pl). We also thank the TIMED/SABER team for providing temperature and OH ver profiles (http://saber.gats-inc.com/index.php).

References

Akiya, Y., A. Saito, T. Sakanoi, Y. Hozumi, A. Yamazaki, Y. Otsuka, M. Nishioka, and T. Tsugawa (2014), First spaceborne observation of the entire concentric airglow structure caused by tropospheric disturbance, *Geophys. Res. Lett.*, *41*(19), 6943–6948, doi:10.1002/2014GL061403.

Azeem, I., J. Yue, L. Hoffmann, S. D. Miller, W. C. Straka, and G. Crowley (2015), Multisensor profiling of a concentric gravity wave event propagating from the troposphere to the ionosphere, *Geophys. Res. Lett.*, *42*(19), 7874–7880, doi:10.1002/2015GL065903.

Bageston, J. V. (2009), Caracterização de ondas de gravidade mesosféricas na estação antártica comandante ferraz, Instituto Nacional de Pesquisas Espaciais, PhD Thesis. [Available at http://urlib.net/8JMKD3MGP7W/ 36FCLLE.]

Franke, P. M., and W. A. Robinson (1999), Nonlinear behavior in the propagation of atmospheric gravity waves, *J. Atmos. Sci.*, *56*(17), 3010–3027.

Franke, S. J., X. Chu, A. Z. Liu, and W. K. Hocking (2005), Comparison of meteor radar and Na doppler lidar measurements of winds in the mesopause region above Maui, Hawaii, *J. Geophys. Res.*, *110*(D9), D09S02, doi:10.1029/2003JD004486.

Fritts, D. C., S. L. Vadas, K. Wan, and J. A. Werne (2006), Mean and variable forcing of the middle atmosphere by gravity waves, *J. Atmos. Sol. Terr. Phys.*, *68*(3–5), 247–265, doi:10.1016/j.jastp.2005.04.010.

Garcia, F. J., M. J. Taylor, and M. C. Kelley (1997), Two-dimensional spectral analysis of mesospheric airglow image data, *Appl. Opt.*, *36*(29), 7374–7385, doi:10.1364/AO.36.007374.

Gardner, C. S., and A. Z. Liu (2007), Seasonal variations of the vertical fluxes of heat and horizontal momentum in the mesopause region at Starfire Optical Range, New Mexico, *J. Geophys. Res.*, *112*, D09113, doi:10.1029/2005JD006179.

Gong, J., J. Yue, and D. L. Wu (2015), Global survey of concentric gravity waves in AIRS images and ECMWF analysis, *J. Geophys. Res. Atmos.*, *120*(6), 2210–2228, doi:10.1002/2014JD022527.

Hines, C. (1960), Internal atmospheric gravity waves at ionospheric heights, *Can. J. Phys.*, *38*, 1441–1481.

Hocking, W., B. Fuller, and B. Vandepeer (2001), Real-time determination of meteor-related parameters utilizing modern digital technology, *J. Atmos. Sol. Terr. Phys.*, *63*, 155–169, doi:10.1016/S1364-6826(00)00138-3.

Li, Z. (2011), An observational investigation on gravity wave characteristics and propagation in the lower stratosphere and mesopause, Univ. of Illinois, PhD Thesis.

Liu, A. Z., and G. R. Swenson (2003), A modeling study of O_2 and OH airglow perturbations induced by atmospheric gravity waves, *J. Geophys. Res.*, *108*(D4), 4151, doi:10.1029/2002JD002474.

Miller, S. D., W. C. Straka, J. Yue, S. M. Smith, M. J. Alexander, L. Hoffmann, M. Setvák, and P. T. Partain (2015), Upper atmospheric gravity wave details revealed in nightglow satellite imagery, *Proc. Natl. Acad. Sci.*, *112*(49), E6728—E6735, doi:10.1073/pnas.1508084112.

Nishioka, M., T. Tsugawa, M. Kubota, and M. Ishii (2013), Concentric waves and short-period oscillations observed in the ionosphere after the 2013 Moore EF5 tornado, *Geophys. Res. Lett.*, *40*(21), 5581–5586, doi:10.1002/2013GL057963.

Pautet, P.-D., M. J. Taylor, A. Z. Liu, and G. R. Swenson (2005), Climatology of short-period gravity waves observed over northern Australia during the Darwin area wave experiment (DAWEX) and their dominant source regions, *J. Geophys. Res.*, *110*, D03S90, doi:10.1029/2004JD004954.

Pendleton, W. R., M. J. Taylor, and L. C. Gardner (2000), Terdiurnal oscillations in OH meinel rotational temperatures for fall conditions at northern mid-latitude sites, *Geophys. Res. Lett.*, *27*(12), 1799–1802, doi:10.1029/2000GL003744.

Perwitasari, S., T. Sakanoi, A. Yamazaki, Y. Otsuka, Y. Hozumi, Y. Akiya, A. Saito, K. Shiokawa, and S. Kawamura (2015), Coordinated airglow observations between IMAP/VISI and a ground-based all-sky imager on concentric gravity wave in the mesopause, *J. Geophys. Res. Space Physics*, *120*(11), 9706–9721, doi:10.1002/2015JA021424.

Sentman, D., E. Wescott, R. Picard, J. Winick, H. Stenbaek-Nielsen, E. Dewan, D. Moudry, F. S. Sabbas, M. Heavner, and J. Morrill (2003), Simultaneous observations of mesospheric gravity waves and sprites generated by a midwestern thunderstorm, *J. Atmos. Sol. Terr. Phys.*, *65*(5), 537–550, doi:10.1016/S1364-6826(02)00328-0.

Smith, S. M., J. Scheer, E. R. Reisin, J. Baumgardner, and M. Mendillo (2006), Characterization of exceptionally strong mesospheric wave events using all-sky and zenith airglow observations, *J. Geophys. Res.*, *111*, A09309, doi:10.1029/2005JA011197.

Smith, S. M., S. L. Vadas, W. J. Baggaley, G. Hernandez, and J. Baumgardner (2013), Gravity wave coupling between the mesosphere and thermosphere over New Zealand, *J. Geophys. Res. Space Physics*, *118*(5), 2694–2707, doi:10.1002/jgra.50263.

Snively, J. B., and V. P. Pasko (2003), Breaking of thunderstorm-generated gravity waves as a source of short-period ducted waves at mesopause altitudes, *Geophys. Res. Lett.*, *30*(24), 2254, doi:10.1029/2003GL018436.

Suzuki, S., K. Shiokawa, Y. Otsuka, T. Ogawa, K. Nakamura, and T. Nakamura (2007), A concentric gravity wave structure in the mesospheric airglow images, *J. Geophys. Res. Atmos.*, *112*, D02102, doi:10.1029/2005JD006558.

Swenson, G. R., and C. S. Gardner (1998), Analytical models for the responses of the mesospheric OH* and Na layers to atmospheric gravity waves, *J. Geophys. Res.*, *103*(D6), 6271–6294, doi:10.1029/97JD02985.

Tang, J., F. Kamalabadi, L. Rumsey, and G. Swenson (2003), Point-source suppression for atmospheric wave extraction from airglow imaging measurements, *IEEE Trans. Geosci. Remote Sens.*, *41*(1), 146–152, doi:10.1109/TGRS.2002.808064.

Tarasick, D. W., and C. O. Hines (1990), The observable effects of gravity waves on airglow emissions, *Planet. Space Sci.*, *38*(9), 1105–1119, doi:10.1016/0032-0633(90)90019-M.

Taylor, M., and M. Hapgood (1988), Identification of a thunderstorm as a source of short period gravity waves in the upper atmospheric nightglow emissions, *Planet. Space Sci.*, *36*(10), 975–985, doi:10.1016/0032-0633(88)90035-9.

Taylor, M., M. Hapgood, and P. Rothwell (1987), Observations of gravity wave propagation in the OI (557.7 nm), Na (589.2 nm) and the near infrared OH nightglow emissions, *Planet. Space Sci.*, *35*(4), 413–427, doi:10.1016/0032-0633(87)90098-5.

Taylor, M. J., W. R. Pendleton, H.-L. Liu, C. Y. She, L. C. Gardner, R. G. Roble, and V. Vasoli (2001), Large amplitude perturbations in mesospheric OH Meinel and 87-km Na lidar temperatures around the autumnal equinox, *Geophys. Res. Lett.*, *28*(9), 1899–1902, doi:10.1029/2000GL012682.

Vadas, S., J. Yue, and T. Nakamura (2012), Mesospheric concentric gravity waves generated by multiple convective storms over the North American Great Plain, *J. Geophys. Res.*, *117*, D07113, doi:10.1029/2011JD017025.

Vadas, S. L., and G. Crowley (2010), Sources of the traveling ionospheric disturbances observed by the ionospheric tiddbit sounder near Wallops Island on 30 October 2007, *J. Geophys. Res.*, *115*, A07324, doi:10.1029/2009JA015053.

Vadas, S. L., and D. C. Fritts (2001), Gravity wave radiation and mean responses to local body forces in the atmosphere, *J. Atmos. Sci.*, *58*(16), 2249–2279, doi:10.1175/1520-0469(2001)058<2249:GWRAMR>2.0.CO;2.

Vadas, S. L., and D. C. Fritts (2002), The importance of spatial variability in the generation of secondary gravity waves from local body forces, *Geophys. Res. Lett.*, *29*(20), 45–1–45–4, doi:10.1029/2002GL015574.

Vadas, S. L., and D. C. Fritts (2004), Thermospheric responses to gravity waves arising from mesoscale convective complexes, *J. Atmos. Sol. Terr. Phys.*, *66*(6–9), 781–804, doi:10.1016/j.jastp.2004.01.025.

Vadas, S. L., D. C. Fritts, and M. J. Alexander (2003), Mechanism for the generation of secondary waves in wave breaking regions, *J. Atmos. Sci.*, *60*(1), 194–214, doi:10.1175/1520-0469(2003)060<0194:MFTGOS>2.0.CO;2.

Vadas, S. L., J. Yue, C.-Y. She, P. A. Stamus, and A. Z. Liu (2009), A model study of the effects of winds on concentric rings of gravity waves from a convective plume near fort collins on 11 May 2004, *J. Geophys. Res.*, *114*, D06103, doi:10.1029/2008JD010753.

Vargas, F., G. Swenson, A. Liu, and D. Gobbi (2007), O(1S), OH, and O_2(b) airglow layer perturbations due to AGWs and their implied effects on the atmosphere, *J. Geophys. Res.*, *112*, D14102, doi:10.1029/2006JD007642.

Vargas, F., D. Gobbi, H. Takahashi, and L. M. Lima (2009), Gravity wave amplitudes and momentum fluxes inferred from OH airglow intensities and meteor radar winds during SpreadFEx, *Ann. Geophys.*, *27*(6), 2361–2369, doi:10.5194/angeo-27-2361-2009.

Xu, J., et al. (2015), Concentric gravity waves over northern China observed by an airglow imager network and satellites, *J. Geophys. Res. Atmos.*, *120*, 11,058–11,078, doi:10.1002/2015JD023786.

Yue, J., S. L. Vadas, C.-Y. She, T. Nakamura, S. C. Reising, H.-L. Liu, P. Stamus, D. A. Krueger, W. Lyons, and T. Li (2009), Concentric gravity waves in the mesosphere generated by deep convective plumes in the lower atmosphere near Fort Collins, Colorado, *J. Geophys. Res.*, *114*, D06104, doi:10.1029/2008JD011244.

Yue, J., L. Hoffmann, and M. Joan Alexander (2013), Simultaneous observations of convective gravity waves from a ground-based airglow imager and the AIRS satellite experiment, *J. Geophys. Res. Atmos.*, *118*(8), 3178–3191, doi:10.1002/jgrd.50341.

Zhao, Y., M. J. Taylor, and X. Chu (2005), Comparison of simultaneous Na lidar and mesospheric nightglow temperature measurements and the effects of tides on the emission layer heights, *J. Geophys. Res.*, *110*, D09S07, doi:10.1029/2004JD005115.

Zhu, X., and J. R. Holton (1987), Mean fields induced by local gravity-wave forcing in the middle atmosphere, *J. Atmos. Sci.*, *44*(3), 620–630, doi:10.1175/1520-0469(1987)044<0620:MFIBLG>2.0.CO;2.